



High-resolution rock abundance derivation of lunar cold spot craters based on RA-SAR model

Jiacheng Sun^{a,b,c}, Xin Lu^{a,b,c}, Gaofeng Shu^{a,b,c,*} ,
Zhengwei Guo^{a,b,c}, Ning Li^{a,b,c}

^a School of Computer and Information Engineering, Henan University, Kaifeng, 475004, China

^b Henan Key Laboratory of Big Data Analysis and Processing, Henan University, Kaifeng, 475004, China

^c Henan Province Engineering Research Center of Spatial Information Processing, Henan University, Kaifeng, 475004, China

ARTICLE INFO

Keywords:

Moon
Rock abundance
Mini-RF
Diviner
Cold spot crater
SAR

ABSTRACT

The distribution of rock abundance (RA) on the lunar surface plays a pivotal role in understanding its geological evolution. This study focuses on the derivation of high-resolution RA data for lunar cold spot craters using Mini-RF (Miniature Radio Frequency) synthetic aperture radar (SAR) data. Firstly, terrain correction was applied to the SAR data. Secondly, the correlation between the Stokes parameters (S_1 , S_2 , S_3 , and S_4) and RA was examined using optically-derived RA data, which aligns with the resolution of the Mini-RF SAR images. By plotting scatter diagrams showing the relationships between the Stokes parameters and the optically-derived RA, strong statistical associations were established. Finally, based on these findings, we formulated a regression-based RA-SAR model. This model was applied to other lunar cold spot craters in order to derive their high-resolution RA distributions. The experimental results show that the model yields highly precise outcomes when validated against both Diviner RA and optical data. The study provides a new approach for inferring rock distribution across the lunar surface using SAR data, and offers valuable insights for advancing lunar geological research.

1. Introduction

Lunar craters are formed by the impacts of meteoroids, asteroids, or comets, causing significant changes to the lunar surface (Hörz et al., 1991; McKay et al., 1991; Stöffler et al., 2006). As key geological features, craters have been a primary focus of scientific investigation (Head et al., 2010; Neish et al., 2014). Cold spot craters, in particular, represent a class of very young and fresh craters recently formed on the Moon, typically less than 3 km in diameter (Williams et al., 2018; Elder et al., 2019). They are referred to as “cold spots” due to the presence of low thermal inertia in their surroundings, a property closely linked to rock abundance (RA), as large rocks have greater thermal inertia compared to fine-grained regolith (Bandfield et al., 2014; Elder et al., 2017; Hayne et al., 2017). Based on this principle, the Lunar Reconnaissance Orbiter (LRO)’s Diviner instrument has derived lunar RA data, which represent the fractional surface area covered by rocks (Paige et al., 2010; Bandfield et al., 2011; Williams et al., 2017). Diviner can detect rocks larger than 1 m in diameter and provides relatively accurate RA data for cold spot craters. However, with a resolution of 240 m/pixel (Bandfield et al.,

2011; Paige et al., 2022; Powell et al., 2023), it is not suitable for detailed quantitative analysis of cold spot craters, most of which are less than 1 km in diameter (Williams et al., 2018). Therefore, higher-resolution RA data is needed to meet the requirements of scientific research.

High-resolution optical images can effectively provide RA data for cold spot craters. Optical data from LRO’s Narrow Angle Camera (NAC) can generate high-resolution RA data by aligning with Diviner rock abundance (Diviner RA), identifying and mapping rocks, adjusting pixel resolution based on Diviner’s pixel scale, and calculating the fractional surface area covered by rocks (Robinson et al., 2010; Wu et al., 2018; Wagner et al., 2024). Although this method can provide accurate high-resolution data, it is labor-intensive and inefficient, making large-scale applications challenging. Moreover, we have found that many cold spot craters on the Moon lack sufficient optical data.

To address this issue, this study utilizes synthetic aperture radar (SAR) data from the Mini-RF instrument aboard LRO (Nozette et al., 2010; Carter et al., 2017). Given its sensitivity to surface roughness, SAR backscatter serves as an effective indicator of lunar rock abundance (Fa

* Corresponding author. School of Computer and Information Engineering, Henan University, Kaifeng, 475004, China.

E-mail address: gaofeng.shu@henu.edu.cn (G. Shu).

and Wieczorek, 2012; Ghent et al., 2014; Gao et al., 2023). A high-resolution RA derivation model is developed based on Mini-RF's polarimetric SAR data. By analyzing the relationship between high-resolution RA data derived from optical methods and Stokes parameters, we establish an RA-SAR model. Mini-RF generates Stokes parameters (S_1, S_2, S_3, S_4) via polarimetric imaging, which describe the electromagnetic wave reflection properties of the lunar surface, offering a unique perspective for analyzing the physical properties of lunar surface materials (Raney et al., 2010; Neish et al., 2011; Calla et al., 2015; Huang et al., 2023). The Mini-RF operates at both X-band and S-band frequencies, with the S-band having a wavelength of 12.6 cm, which enables limited penetration into the lunar regolith. Previous studies have shown that Mini-RF can typically penetrate only a few centimeters to several tens of centimeters beneath the lunar surface, depending on the dielectric properties of the regolith (Nozette et al., 2010; Carter et al., 2012). Given this shallow penetration depth, the SAR signal is primarily influenced by the physical characteristics of the lunar surface. Therefore, rocks buried beneath the surface (including those in the near-surface and deeper layers) have minimal impact on the surface backscatter signal and can be considered negligible in this study. The RA-SAR model will be used to invert the high-resolution RA of cold spot craters on the Moon, providing new data to support the study of lunar surface material distribution and impact craters, as well as offering critical geological information for future lunar exploration missions.

The remainder of this paper is organized as follows: Section 2 introduces the data and fundamental theory used, Section 3 presents the proposed methodology, Section 4 details the experimental results, Section 5 provides the discussion, and Section 6 concludes the study.

2. Dataset and fundamental theories

The parameters of the LROC NAC data, Mini-RF SAR data, and Diviner RA data used in this study are presented in Table 1.

2.1. LROC NAC, Mini-RF SAR and diviner RA

The Narrow Angle Camera (NAC) onboard the Lunar Reconnaissance Orbiter Camera (LROC) consists of two cameras, NAC-L and NAC-R. In full-resolution mode, image data are composed of a series of continuous lines, with up to 52,224 lines and 5000 samples per line. The calibrated NAC image data are stored in 16-bit format, with an imaging altitude of 50 km and a maximum resolution of 0.5 m/pixel (Robinson et al., 2010; Wu and Liu, 2017). This high-resolution imaging capability enables precise identification, mapping, and analysis of rocks on the lunar surface.

The Mini-RF instrument is a hybrid dual-polarization SAR that transmits circularly polarized electromagnetic waves while coherently receiving two orthogonal linearly polarized electromagnetic waves (Nozette et al., 2010; Raney et al., 2010; Cahill et al., 2014). The unique backscattering characteristics of blocky ejecta, such as rocks, result in strong echo halos in the SAR images of cold spot craters (Campbell, 2012; Fa and Cai, 2013). The SAR data used in this study are presented in the form of Stokes parameters, which are calculated as follows.

Table 1
Parameters of the data used in this study.

| Parameters | Unit | LRO NAC | LRO Mini-RF | Diviner RA |
|------------------------|-------------------------|----------------------------|-------------|--------------------------|
| Incidence Angle | Degree | 43.4 | 52.1638 | 40–70 |
| Wavelength | $\mu\text{m}/\text{cm}$ | 0.4–0.76 (μm) | 12.6 (cm) | 13–400 (μm) |
| Resolution | m/pixel | 1.1 | 14.8 | 240 |

$$\begin{bmatrix} S_1 \\ S_2 \\ S_3 \\ S_4 \end{bmatrix} = \begin{bmatrix} \langle |E_{HL}|^2 + |E_{VL}|^2 \rangle \\ \langle |E_{HL}|^2 - |E_{VL}|^2 \rangle \\ 2\text{Re}\langle E_{HL}E_{VL}^* \rangle - 2\text{Im}\langle E_{HL}E_{VL}^* \rangle \end{bmatrix} \quad (1)$$

Here, S_1 represents the total power of the horizontal and vertical components, indicating the total backscatter intensity. It typically reflects the roughness and reflectivity of the target, making it the most directly indicative parameter of surface features in RA modeling, thus contributing the most to the model (Raney et al., 2010; Carter et al., 2012). S_2 represents the differential power between the horizontal and vertical components, revealing the anisotropy and polarization characteristics of the target, which aids in distinguishing rocks from fine-grained regolith. S_3 represents the real part of the complex correlation between the horizontally and vertically polarized components of the received signal, corresponding to the cosine of their average phase difference. S_4 represents the imaginary part, corresponding to the sine of the average phase difference. Together, these two parameters characterize the polarization state of the backscattered wave (Raney, 2006, 2019; Kumari and Bhardwaj, 2020).

The Diviner instrument utilizes nighttime multispectral infrared observations to provide RA data through thermal emission measurements (Bandfield et al., 2011, 2017). Compared to the fine-grained regolith, rocks exhibit higher thermal inertia. Warmer rocks within Diviner's field of view cause an increase in the temperature of the short-wave channels, allowing the simulation of RA based on these temperature variations. As a result, multispectral observations can be used to infer sub-pixel RA at a resolution of 240 m/pixel.

2.2. Lunar cold spot craters

Cold spot craters represent a class of very young and fresh lunar impact features characterized by their distinctive thermal and radar properties. Fig. 1 shows a cold spot crater on the lunar surface.

Fig. 1b and c respectively present the optical and SAR images of the cold spot crater. In optical images, cold spot craters show a bright central region at the proximal area, while the distal region appears relatively darker. This contrast is due to the redistribution of surface materials caused by the impact, which alters the thermal and optical properties of the surface. In SAR images, the proximal ejecta of cold spot craters usually exhibit stronger radar backscatter, while the distal ejecta show relatively weaker returns. This backscatter pattern is related to differences in surface roughness and rock abundance caused by the impact event.

2.3. The ejection range of rocks

Fig. 2 presents a schematic diagram of the formation of a cold spot crater. For cold spot craters, which are exceptionally young and fresh, the RA in the surrounding area is primarily associated with exposed surface rocks, as the proximal ejecta layer's rocks have not yet decomposed or been buried (Elder et al., 2019). The extent of rock distribution is constrained by the local regolith thickness, as lunar regolith typically has a significant influence on the ejection velocity of bedrock fragments during impact events (Bart and Melosh, 2010a). Specifically, the presence of regolith reduces the ejection velocity of bedrock debris, while the ejection velocity of regolith fragments tends to be higher, resulting in greater ejection distances. In contrast, bedrock fragments, produced by bedrock impacts, exhibit relatively lower velocities and shorter ejection distances. Most cold spot craters exhibit a bowl-shaped morphology, indicating that the impact angle is close to 90° , which leads to a crown-like distribution of ejected rocks. Therefore, the ejection range D of rocks produced by bedrock impacts at lunar cold spot craters can be determined (Fig. 2).

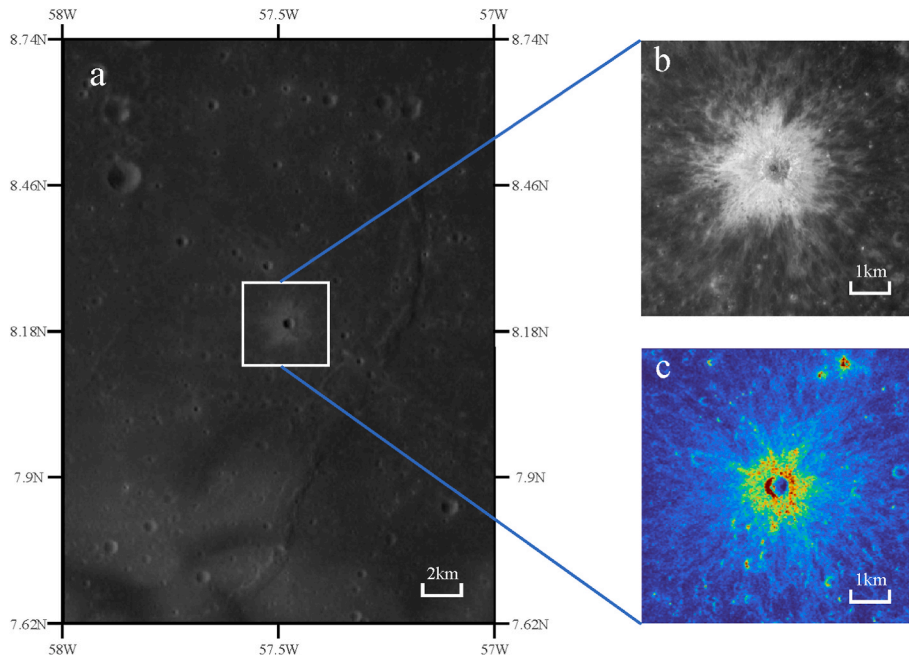


Fig. 1. The cold spot craters schematic diagram.

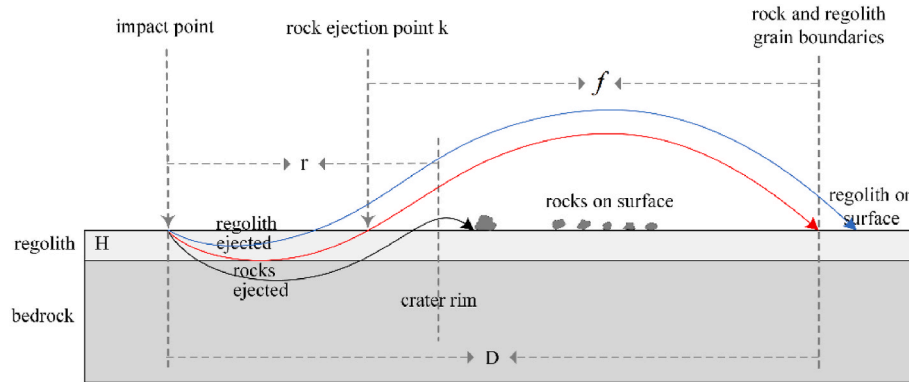


Fig. 2. Schematic diagram of the formation of a cold spot crater. In this illustration, a boundary between the fine-grained regolith and rocks is established, assuming that the minimum size of rocks considered is 1 m, with smaller rocks excluded. During the formation of the cold spot crater, r represents the crater radius, R is the transient crater radius, f is the distance the rocks are ejected, and D is the distance from the rocks to the center of the crater.

Given that D is considerably smaller than the radius of the Moon, the ejection velocity of the rock is calculated here using the ballistic equation of the object in the plane. The equation is as follows:

$$f = \left(\frac{v^2}{g}\right) \sin(2\theta) \quad (2)$$

where f represents the horizontal distance the rock travels, v is the ejection velocity of the rock, g is the acceleration of lunar gravity, and θ is the Angle of the ejection of the rock. It is assumed that each rock is thrown out at an angle of 45° from the horizontal line (Cintala et al., 1978). This assumption is reasonable given that for major ejection flows, the ejection angle is typically close to 45° (with a range of $\pm 15^\circ$), and the dependence of the ejection velocity function on the ejection angle is weak in this range. Consequently, the equation is reduced to the following form:

$$f = \frac{v^2}{g} \quad (3)$$

It is not possible to assume that all rocks are ejected from the same radial position inside the crater, so a simple ballistic equation cannot be

used to solve for velocity. Therefore, based on the scaling theory of impact crater formation (Richardson et al., 2005), the ejection velocity of bedrock is calculated.

$$v = \frac{2\sqrt{Rg}}{1+\epsilon} \left(\frac{r}{R}\right)^{-\epsilon} - \frac{2\sqrt{Rg}}{1+\epsilon} \left(\frac{r}{R}\right)^\lambda \quad (4)$$

where R represents the transient crater radius, the value is 0.85 of the final crater radius (Bart and Melosh, 2010b); ϵ denotes the material parameter, r is the crater radius as a function of time during the crater formation stage, and λ is the model parameter. Particularly, $\epsilon = 1.5$, $\lambda = 10$ for basalt on the Moon (Housen et al., 1983).

The distance D from the rock to the center of the crater is equal to the radius of the crater plus the distance thrown by the bedrock. This can be express as follows:

$$D = r + f \quad (5)$$

The approximate distribution range of rocks surrounding the cold spot crater can be calculated using the above Eqs. (2)–(5).

3. Methods

In this study, a cold spot crater located in the lunar mare was selected as the experimental target, and the study area is shown in Fig. 3.

The study area, situated in the central part of Oceanus Procellarum and adjacent to the Herodotus crater, formed geologically between approximately 3.69 and 1.17 Ga (Hiesinger et al., 2003). This region has undergone multiple volcanic episodes, including at least five major eruptions (Zhang et al., 2024). The surrounding terrain, shaped by both volcanic and impact processes, exhibits characteristic features such as low albedo and high-Ti basalt distribution (Mustard et al., 2011), indicating a geologically complex and relatively young surface. These geological attributes provide valuable context for understanding the age and evolution of the study area.

3.1. Flowchart of the proposed method

The objective of this study is to derive high-resolution RA for other cold spot craters by establishing a relationship model between optically-derived high-resolution RA and SAR data. The flowchart of the proposed method is shown in Fig. 4. The first step involves data processing, where Diviner RA, NAC, and Mini-RF SAR data are pre-processed. Next, optical data are used to derive RA at a resolution consistent with Mini-RF SAR, and SAR data are used to calculate Stokes parameters. In the following step, correlation analysis is performed, and a model is established. We analyze the correlation between the high-resolution RA and Stokes parameters and develop the RA-SAR relationship model based on this analysis. This model is then applied to derive high-resolution RA for other cold spot craters. Finally, the derived results are validated and analyzed through two methods. In Method 1, the high-resolution RA is downsampled to match the resolution of the Diviner RA for comparison. In Method 2, optical data are used for validation by randomly selecting regions, deriving RA for those areas using optical data, and then comparing the results.

3.2. Optical data processing

Before establishing the model, it is necessary to obtain RA data that matches the resolution of Mini-RF SAR. High-resolution RA is derived using NAC optical data, with a cold spot crater on the lunar mare selected as the derivation target. Following the method described above, the distribution range of rocks around the cold spot crater is calculated using Eqs. (2)–(5), resulting in a range of 3.05 km. In this study, the optical data used have a resolution of 1.1 m/pixel, which limits the ability to detect small rocks. To ensure reliable identification, only rock ≥ 4 pixels in diameter were labeled. As a result, the labeled range is smaller than the theoretical value. As shown in Fig. 5.

3.2.1. Rock labeling and statistics

In this study, rocks within the determined distribution range are labeled. Using ArcGIS Pro software and NAC data, rocks surrounding the cold spot crater are identified and labeled, resulting in a total of over 11,000 labeled rocks. The detailed processing workflow is illustrated in Fig. 6.

The labeled rock statistics around the cold spot crater are shown in Table 2.

The calculated extent of ejected rocks from the crater with sizes exceeding 1 m is 3.05 km, within which rocks are identified and labeled. Due to the limitations imposed by the resolution of the optical images, the final identified rock distribution is necessarily smaller than 3.05 km. In this case, the rock distribution extent labeled in the optical images is 2.45 km, approximately two and a half crater diameters, consistent with the typical rock distribution range around craters of this type, which extends 2–3 crater diameters (Venkatraman et al., 2023). The discrepancy between the labeled range and the previously calculated ejecta range arises from the differences in rock size considered in each case. The ejecta range estimates the distribution of rocks with a diameter of 1 m, while the labeled range includes rocks with a diameter of 4.4 m. This distinction is based on the resolution of the NAC data used, which is 1.1 m/pixel. To minimize human error, only rocks with sizes greater than or equal to 4 pixels were labeled. Fig. 7 shows a diagram of rock labeling using NAC data and the results after co-registration with Diviner RA.

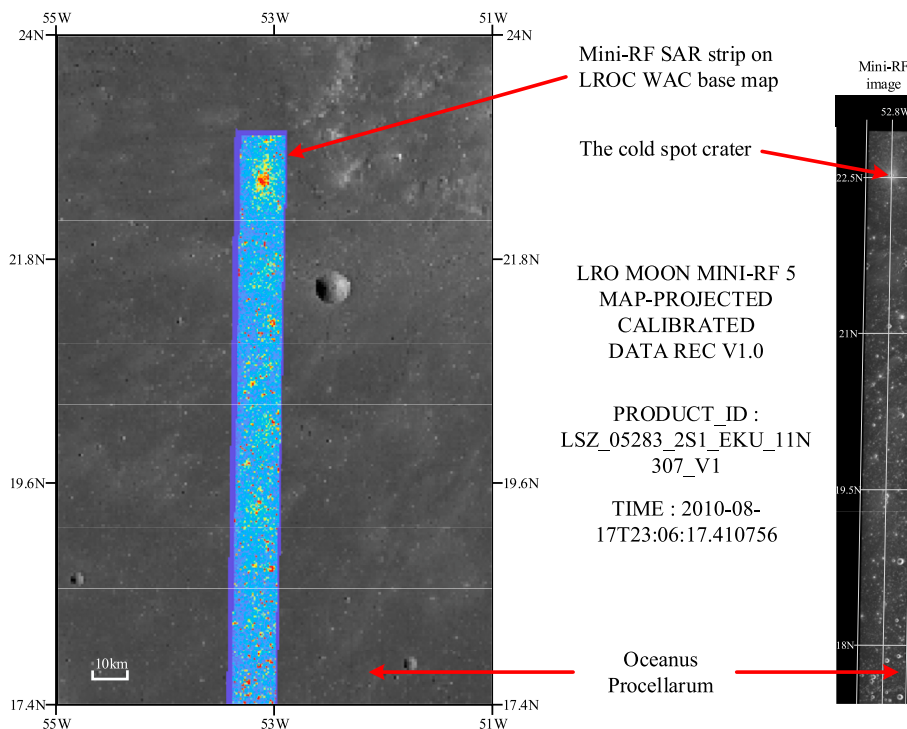


Fig. 3. The SAR data coverage area.

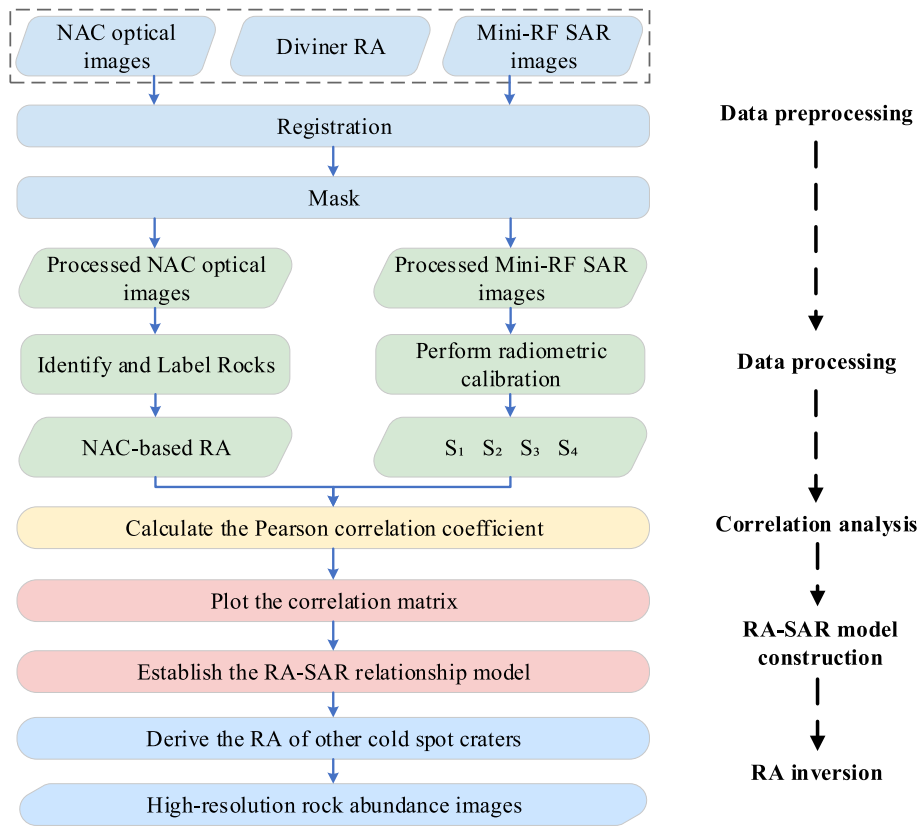


Fig. 4. Flowchart of the proposed methodology.

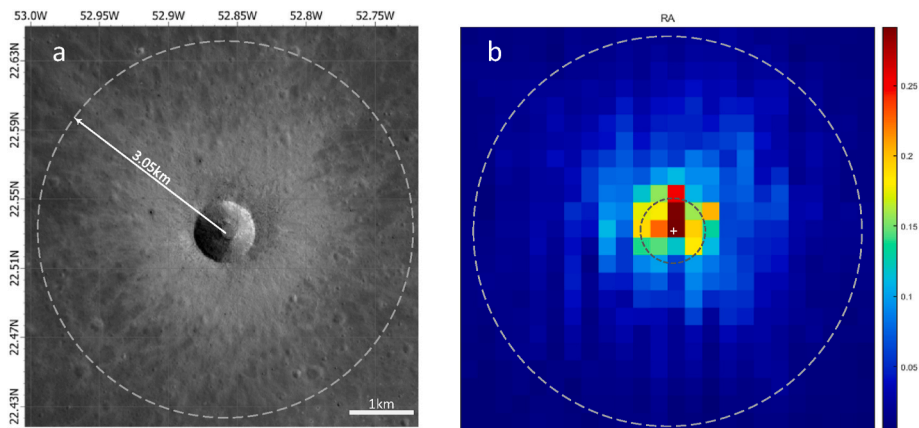


Fig. 5. Cold spot crater required for optical derivation of RA. (a) A mosaic composed of two NAC images (M1191046036LE, M1191046036RE). (b) The Diviner RA (RA_SAM_70Sto70N.tif).

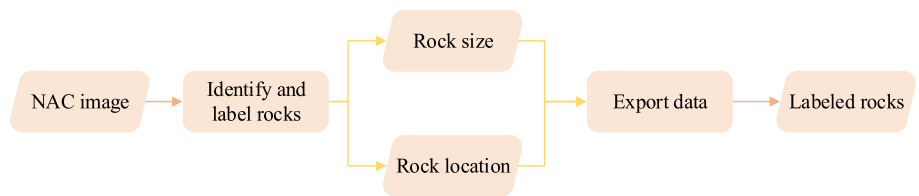


Fig. 6. The process of labelling rock.

3.2.2. Rock abundance derived from NAC

By using the resolution of Diviner RA as a reference, individual pixel units of RA were divided into smaller segments, and the rock surface

area fraction within the processed pixel units was subsequently calculated (Fig. 8). This method allowed us to obtain high-resolution RA data. We generated RA datasets at resolutions of 60 m/pixel (Fig. 9a) or 15 m/

Table 2
Statistical information of the rocks.

| Size [m] | Cumulative number | Cumulative number [km ²] |
|----------|-------------------|--------------------------------------|
| 4.4 | 5196 | 299.14 |
| 5.5 | 2583 | 148.75 |
| 6.6 | 1344 | 76.94 |
| 7.7 | 735 | 42.08 |
| 8.8 | 428 | 24.64 |
| 9.9 | 265 | 15.26 |
| 11.0 | 180 | 10.38 |
| 12.1 | 126 | 7.26 |
| 13.2 | 88 | 5.09 |
| 14.3 | 56 | 3.22 |
| 15.4 | 39 | 2.28 |
| 16.5 | 27 | 1.59 |
| 17.6 | 10 | 0.58 |
| 18.7 | 4 | 0.228 |

pixel (Fig. 9b), with Fig. 9b matching the resolution of the Mini-RF SAR data. This dataset will be utilized in the next step to establish the RA-SAR relationship mode.

The schematic diagram in Fig. 8 above illustrates the steps for deriving RA data at different resolutions generated by Diviner RA. Using the methods and labeled rock data in this diagram, we can calculate RA data at various resolutions for cold spot craters.

3.3. Perform radiometric calibration

The local incidence angle (LIA) variations and terrain-induced brightness fluctuations in SAR images can introduce errors in the correlation analysis. Due to the presence of crater walls, SAR data within

lunar craters are significantly affected by topographic variations. In contrast, the terrain outside the crater is relatively flat, resulting in weaker topographic effects. The interior of the crater was not used in this study. To mitigate these effects, we adopted the terrain correction approach proposed by Huang et al. (2023), which compensates for incidence angle variations caused by topography based on DEM data. This method effectively reduces the influence of terrain effects on the Mini-RF SAR polarization parameters and achieves a relative decoupling between the two.

Specifically, the method calculates the LIA for each pixel using DEM data. First, the surface normal vector is estimated within a 3×3 elevation window by fitting a local plane, and the angle between this normal and the radar incidence direction is computed to derive the LIA. All pixels are then grouped according to their LIA values, and the average SAR value is calculated within each LIA interval. This enables statistical analysis of the relationship between LIA and each Stokes parameter (S1–S4), and the derivation of their respective trends with respect to LIA. Finally, to further mitigate terrain effects, the method normalizes the observed SAR values by expressing them as deviations relative to the mean value within each LIA interval. This reduces the impact of incidence angle variations on SAR brightness and allows the SAR parameters to better reflect the surface scattering characteristics.

Following the application of the above method, the Mini-RF SAR data used in this study were radiometrically corrected to reduce brightness variations caused by local topography. Fig. 10 displays the resulting terrain-corrected SAR parameter images. Specifically, Fig. 10 (a₁), (b₁), (c₁), and (d₁) show the Stokes parameter images prior to terrain correction; Fig. 10(a₂), (b₂), (c₂), and (d₂) show the corresponding images after terrain correction. Fig. 10(a₃), (b₃), (c₃), and (d₃)

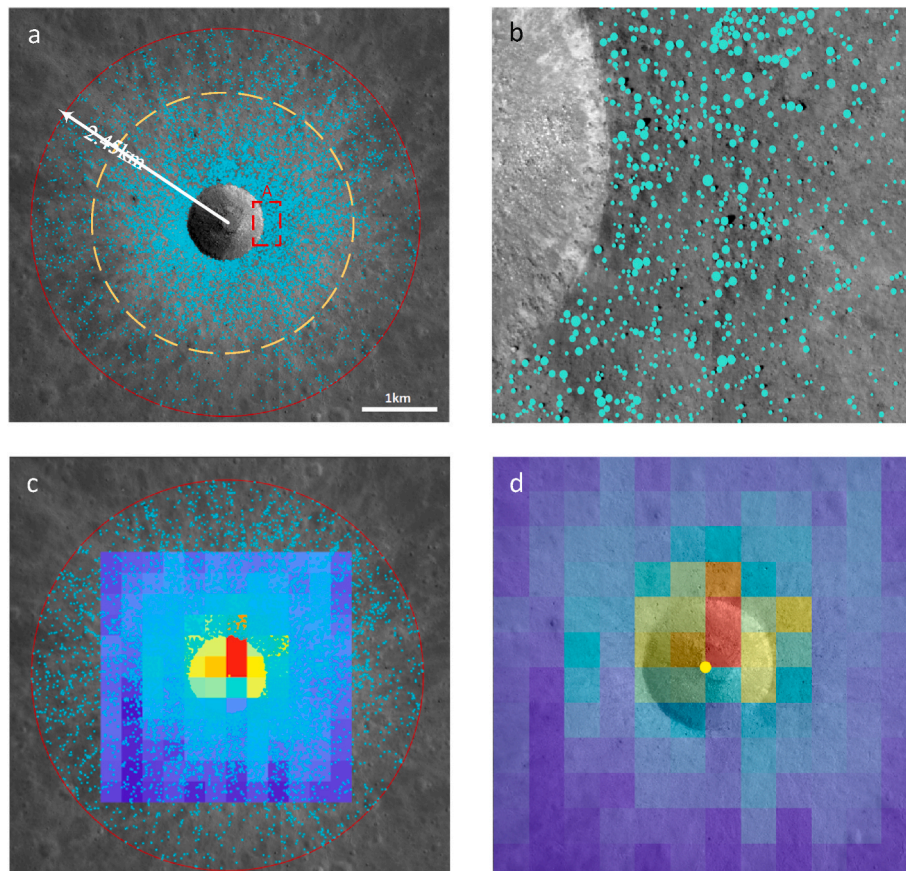


Fig. 7. (a) Is a schematic diagram of rock labeling, where the red circle indicates the labeled area and the yellow circle represents the distribution range of proximal rocks. (b) Shows an enlarged view of the rock distribution corresponding to the red box A in (a). (c) Presents the registration result between Diviner RA and NAC, focusing only on the proximal rock distribution around the crater. (d) Displays the result image after registration of the selected area.

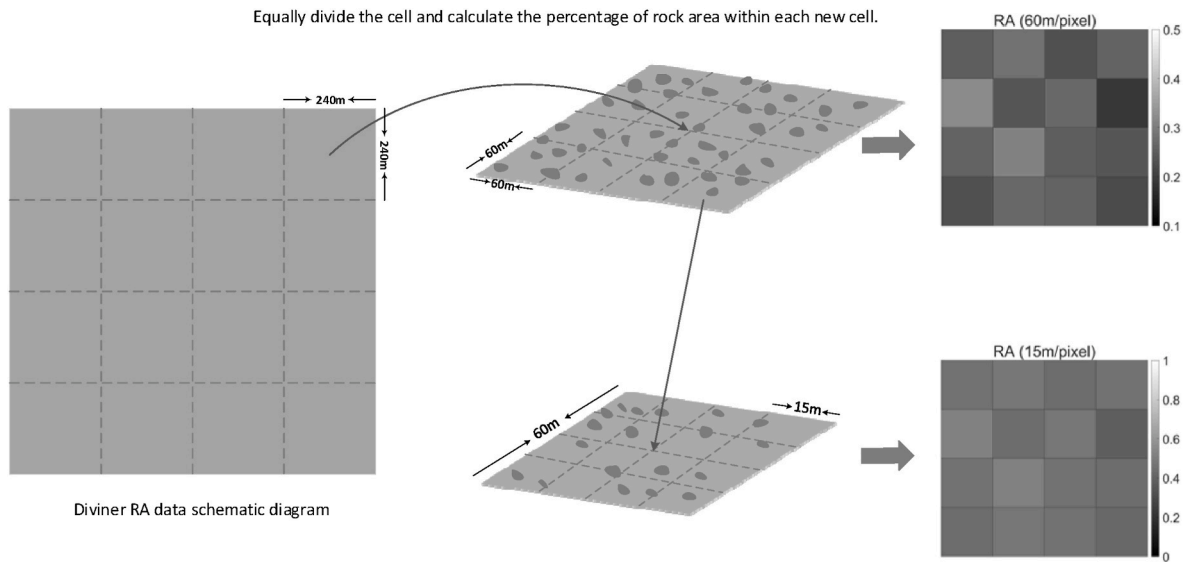


Fig. 8. Schematic diagram of calculating RA at different resolutions.

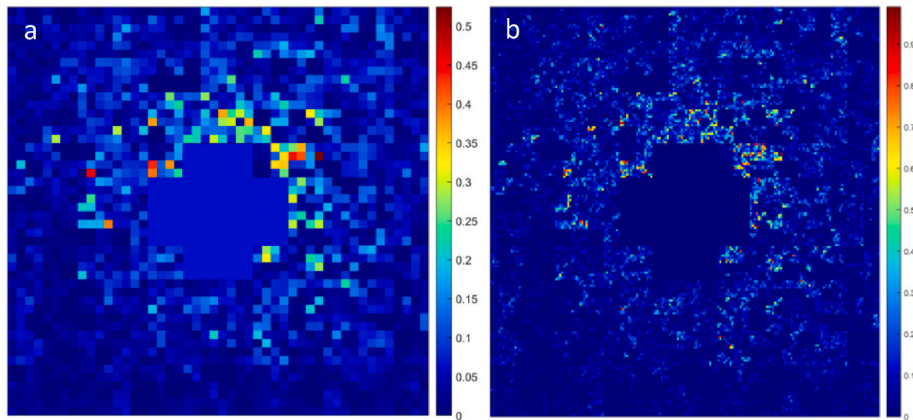


Fig. 9. (a) RA at 60m/pixel resolution. (b) RA at 15m/pixel resolution.

represent the near-crater regions, with the interior areas of the crater masked out. As shown in Fig. 10, the topographic effects on SAR brightness have been significantly mitigated.

3.4. Correlation analysis

Based on Sections 3.2 and 3.3, scatter plots between RA and the four Stokes parameters were generated. Different function forms were employed to fit the data, including linear, polynomial, and exponential functions, to model the relationship between RA and the Stokes parameters, with the corresponding R^2 values calculated for each fit. The optimal values were then selected, and Pearson correlation coefficients between the different feature parameters were computed to construct a correlation matrix. Finally, the weights of each Stokes parameter relative to RA were determined, and a linear weighted regression model was constructed based on these weights. Table 3 presents the results of fitting the relationship between RA and the Stokes parameters using three different functions, along with their corresponding R^2 values. Fig. 11 shows the scatter plots of the fitted relationships between RA and the Stokes parameters.

Here, we found that the R^2 values for S_1 , S_2 , S_3 , and S_4 , when fitted with a linear function, were the highest, indicating the best fit. This suggests a linear correlation between RA and the Stokes parameters, as represented by the red line in the scatter plots in Fig. 11. Therefore, a

linear function will be used to establish the relationship model between the two.

3.5. RA-SAR model construction

By analyzing the correlation between RA and Stokes parameters, the correlation matrix is constructed, and the results are shown in Fig. 12. The correlation matrix indicates a decreasing trend in the correlation between RA and the Stokes parameters S_1 , S_2 , S_3 , and S_4 , with S_1 exhibiting the strongest correlation (up to 0.91) and S_4 the weakest (around 0.54). This trend is consistent with the polarization characteristics of electromagnetic waves.

Based on the correlation matrix, the R^2 values of each Stokes parameter were normalized using Eq. (6), resulting in the calculation of the respective weights. These weights represent the relative contribution of each parameter to the RA. The RA-SAR relationship model was then constructed using Eq. (7). This method employs a multi-parameter linear weighted model, effectively integrating the influence of each parameter on RA.

$$W_{S_i} = \frac{R_{S_i}^2}{R_{S_1}^2 + R_{S_2}^2 + R_{S_3}^2 + R_{S_4}^2}, i = 1, 2, 3, 4 \quad (6)$$

$$RA = W_{S_1} \times S_1 + W_{S_2} \times S_2 + W_{S_3} \times S_3 + W_{S_4} \times S_4 \quad (7)$$

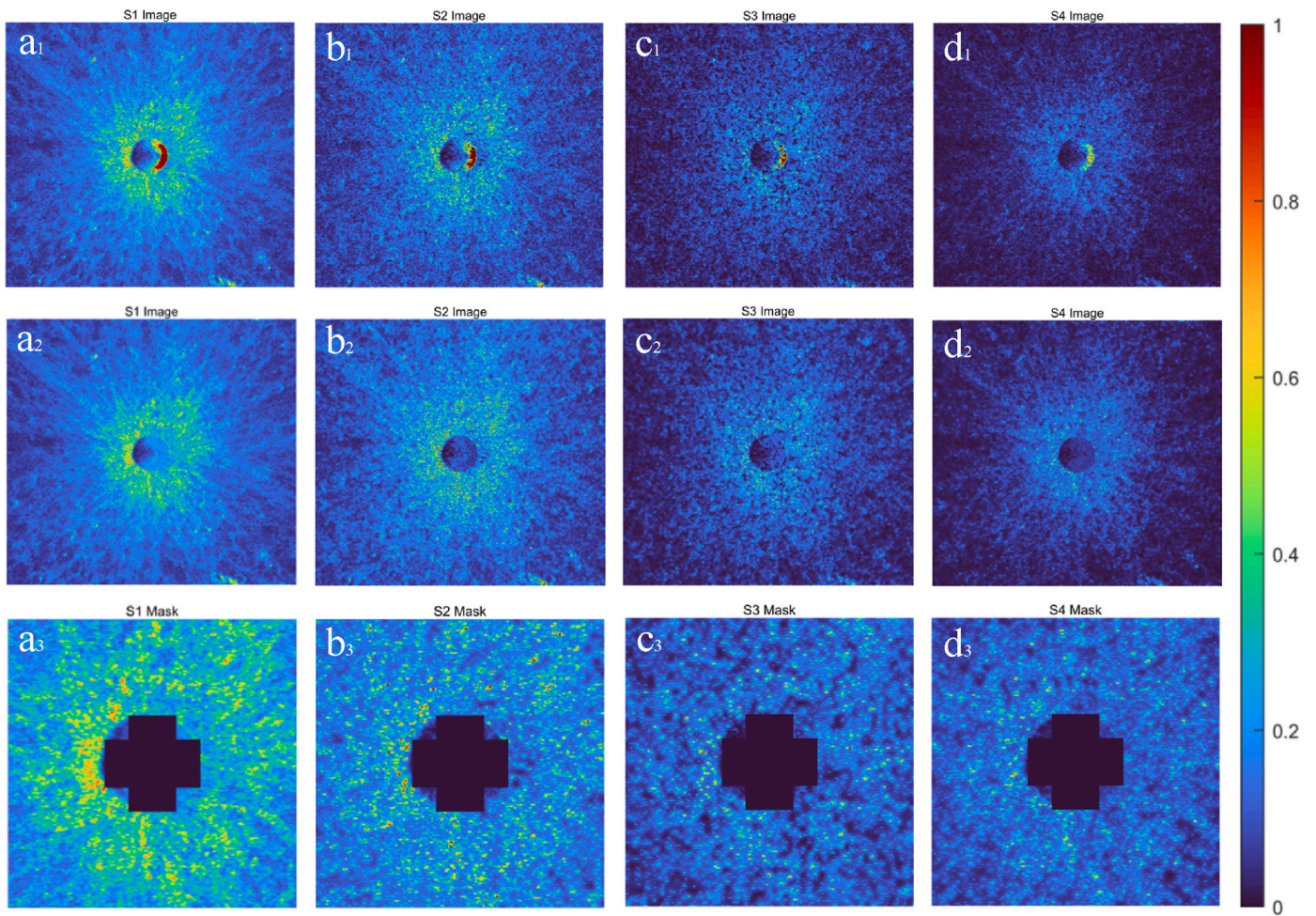


Fig. 10. The terrain-corrected SAR image. (a₁), (b₁), (c₁), and (d₁) show the Stokes parameter images prior to terrain correction. (a₂), (b₂), (c₂), and (d₂) show the Stokes parameter images after terrain correction. (a₃), (b₃), (c₃), and (d₃) show the Stokes parameter images after registration, alignment, and cropping to match the spatial extent of the optically derived RA data.

Table 3

The R^2 values for the relationships between RA and the Stokes parameters were obtained by fitting linear, polynomial, and exponential functions, respectively.

| | S ₁ | S ₂ | S ₃ | S ₄ |
|--------------------------------|----------------|----------------|----------------|----------------|
| RA (Linear Fit (R^2)) | 0.83 | 0.69 | 0.51 | 0.34 |
| RA (Polynomial Fit (R^2)) | 0.7 | 0.63 | 0.5 | 0.27 |
| RA (Exponential Fit (R^2)) | 0.67 | 0.58 | 0.48 | 0.26 |

Here, $R_{S_1}^2$, $R_{S_2}^2$, $R_{S_3}^2$, and $R_{S_4}^2$ represent the R^2 values corresponding to each Stokes parameter, and W_{S_i} denotes the associated weights. Therefore, we employ this weighted model to derive RA (Eq. (7)), where W_{S_1} , W_{S_2} , W_{S_3} , and W_{S_4} values decrease sequentially. Given the SAR image of a cold spot crater, the Stokes parameters can be derived from the SAR image and then substituted into Eq. (7) to obtain the RA data for the crater.

4. Result

4.1. Flowchart of the validation method employed

This study validates the accuracy of the RA-SAR model using the flowchart in Fig. 13. First, RA is derived using the model, then down-sampled and compared with Diviner RA to obtain the first accuracy value. Second, the RA derived from NAC data is compared with the

model-derived RA to calculate the second accuracy value. These two accuracy assessments together verify the reliability of the model.

4.2. Rock abundance derivation

To validate the accuracy of the model, two cold spot craters were selected as targets for RA derivation. The specific information about these craters is provided in Table 4. These two craters are representative, with diameters of 0.7 km and 0.43 km, making them suitably sized for detailed analysis at high resolution. This ensures that the model can be reliably applied across craters of varying scales. Additionally, the distinct cold spot characteristics of these craters facilitate the validation of the model's accuracy in deriving RA.

The corresponding SAR images and Diviner RA images are shown in Fig. 14. Specifically, Figs. 14c–d display the RA maps of Crater A and Crater B, respectively, at a resolution of 240 m/pixel. However, due to the limited number of pixels, detailed quantitative analysis of the craters is not feasible.

Based on the aforementioned RA-SAR model, the high-resolution RA for Crater A and Crater B was derived. The results are shown in Fig. 15. The resolution of RA has been significantly improved, enabling more detailed observation and analysis of the rock distribution characteristics surrounding the crater.

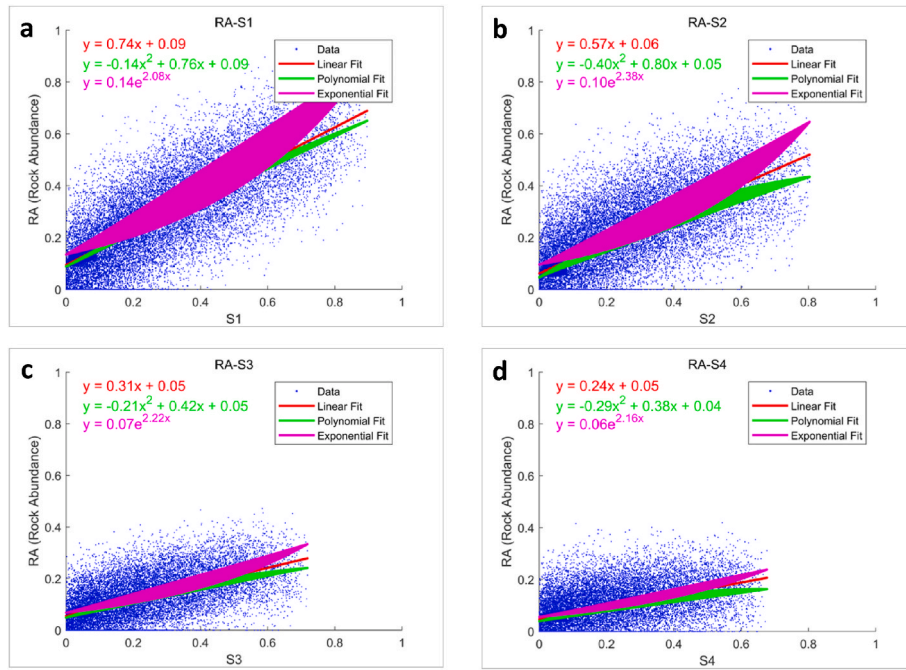


Fig. 11. Scatter plots between RA and Stokes parameters.

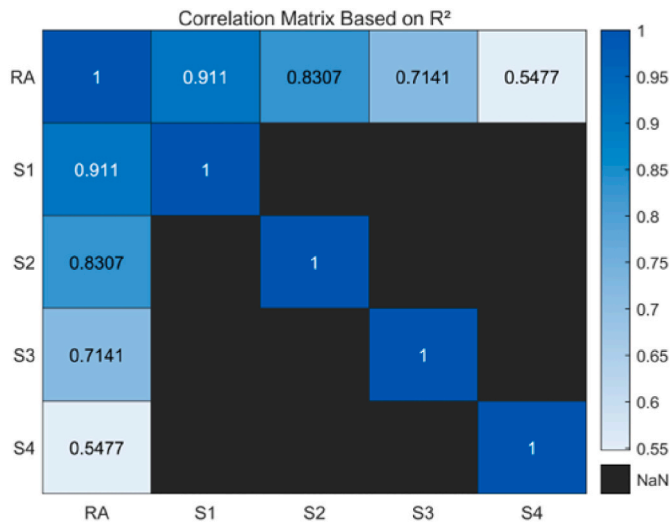


Fig. 12. Correlation matrix between RA and Stokes parameters.

4.3. Diviner RA data validation

In this study, the derived high-resolution RA data were downsampled to match the resolution of the Diviner RA dataset. The down-sampling here is achieved based on the inverse process illustrated in Fig. 8. A row-priority comparison was then conducted between the two datasets. The comparison results are shown in Fig. 16c–g, where the blue line represents the Diviner RA and the red line represents the downsampled RA. Except for a few points, the differences between the two datasets are minimal (Fig. 16c and g). Fig. 16d–h shows the difference values between the two datasets in Fig. 16c–g, respectively. The red boxed areas represent the crater interiors, where significant differences are observed. This discrepancy arises because the model does not incorporate information specific to the crater interior during construction, leading to notable differences in RA within the crater compared to Diviner RA. However, outside the crater, the differences are minor, indicating that the RA-SAR model provides a reliable RA derivation for cold spot

craters.

Here, we use Eq. (8) below to evaluate the overall accuracy of the model-derived RA.

$$Accuracy_{overall} = \frac{1}{N} \sum_{i=1}^N \left(1 - \frac{|RA_{model,i} - RA_{Diviner,i}|}{RA_{Diviner,i}} \right) \times 100\% \quad (8)$$

In this, $RA_{model,i}$ represents the model-derived RA value for the i -th pixel, $RA_{Diviner,i}$ represents the Diviner RA data value for the i -th pixel, and N denotes the total number of pixels. After calculating the accuracy for each pixel (excluding pixels within the cold spot crater interior), the overall model accuracy is obtained by averaging the accuracy values across all pixels. Using Eq. (8), the accuracy of the derived RA for Crater A and Crater B was evaluated, yielding results exceeding 90 % (Table 5). This indicates that the model achieves high accuracy in deriving RA for cold spot craters.

4.4. Optical data validation

To further validate the accuracy of the model, optical data was employed to verify the derivation results. Using NAC optical imagery, three random areas around Crater A and Crater B were selected. The rocks within the selected regions were labeled, and the corresponding RA was calculated. The calculated RA was then compared with the model-predicted RA for each respective area, and a detailed accuracy analysis was performed. The results are shown in Fig. 17.

In the three randomly selected regions, rocks in the optical images were labeled, and RA values were calculated. These values were then compared with those in the corresponding regions of the model-derived RA image. Using an approach similar to that in Eq. (8), accuracy metrics were obtained, as shown in Table 6. The high calculated accuracy indicates that the model demonstrates strong precision and reliability. Table 6 presents the results of optical validation. It was observed that the model's predicted RA is more accurate in areas closer to the crater, while the accuracy decreases in regions farther from the crater. This trend aligns with the distribution pattern of rocks around cold spot craters, where rock density decreases with increasing distance from the crater center.

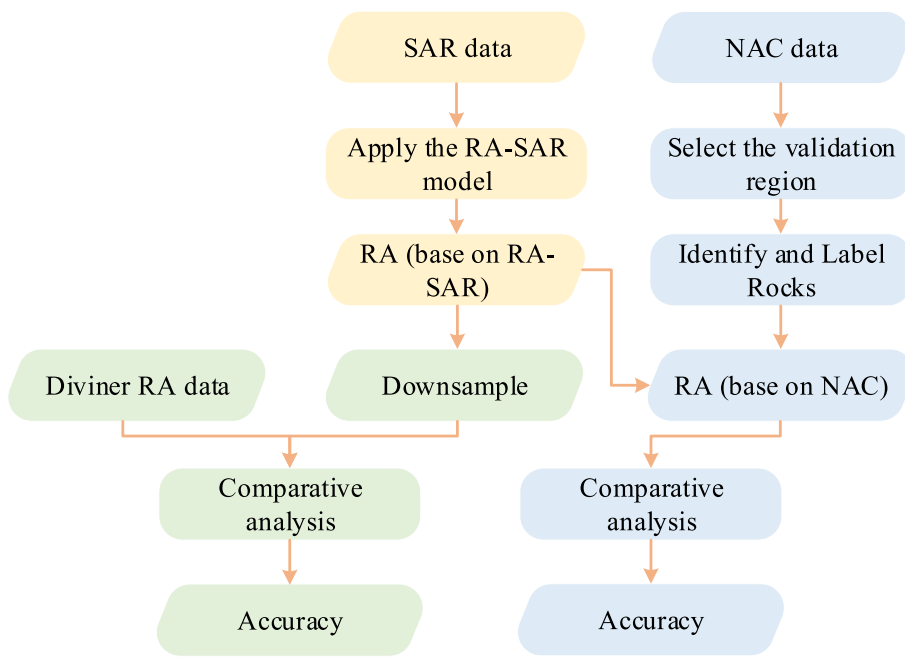


Fig. 13. The flowchart of model validation.

Table 4

Information on the two selected cold spot craters.

| | Crater A | Crater B |
|------------------------|--------------|---------------|
| Latitude and Longitude | 8.67N 45.06W | 12.61N 45.14W |
| Diameter | 0.7 km | 0.43 km |

5. Discussion

Regarding the model's effectiveness, we employed Mini-RF SAR data and established a high-resolution RA-SAR derivation model based on the correlation between the Stokes parameters and optically derived RA data. By comparing the model-predicted RA with the Diviner RA data, we observed a high degree of agreement. Compared to existing

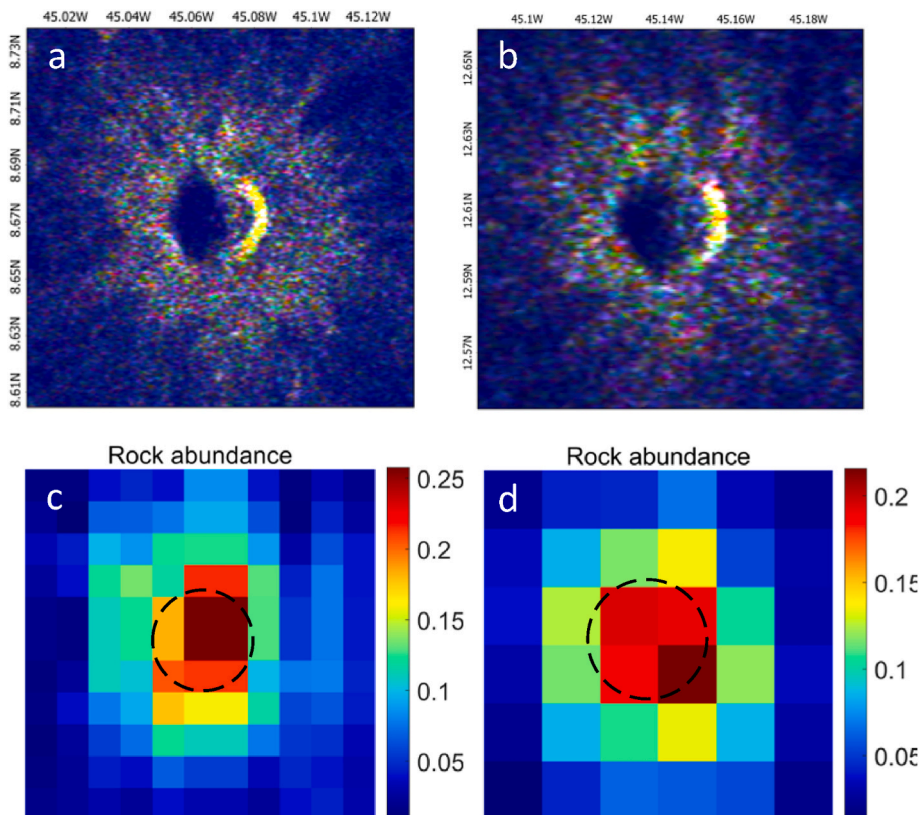


Fig. 14. SAR data and Diviner RA data of Crater A and Crater B.

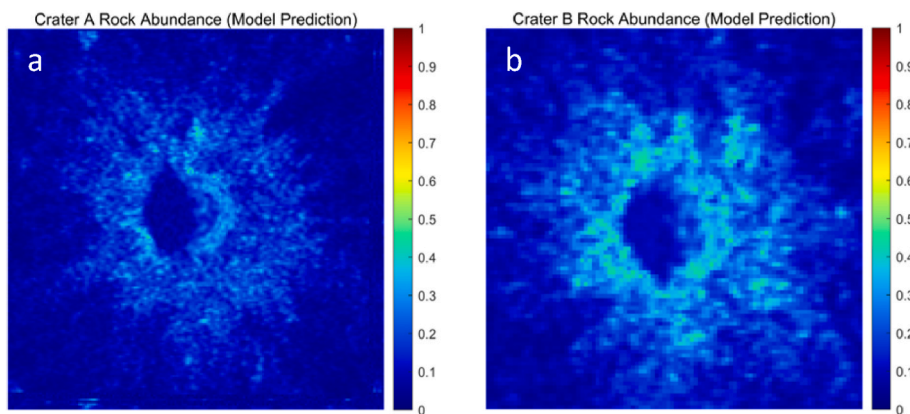


Fig. 15. High-resolution RA derivation results (15m/pixel).

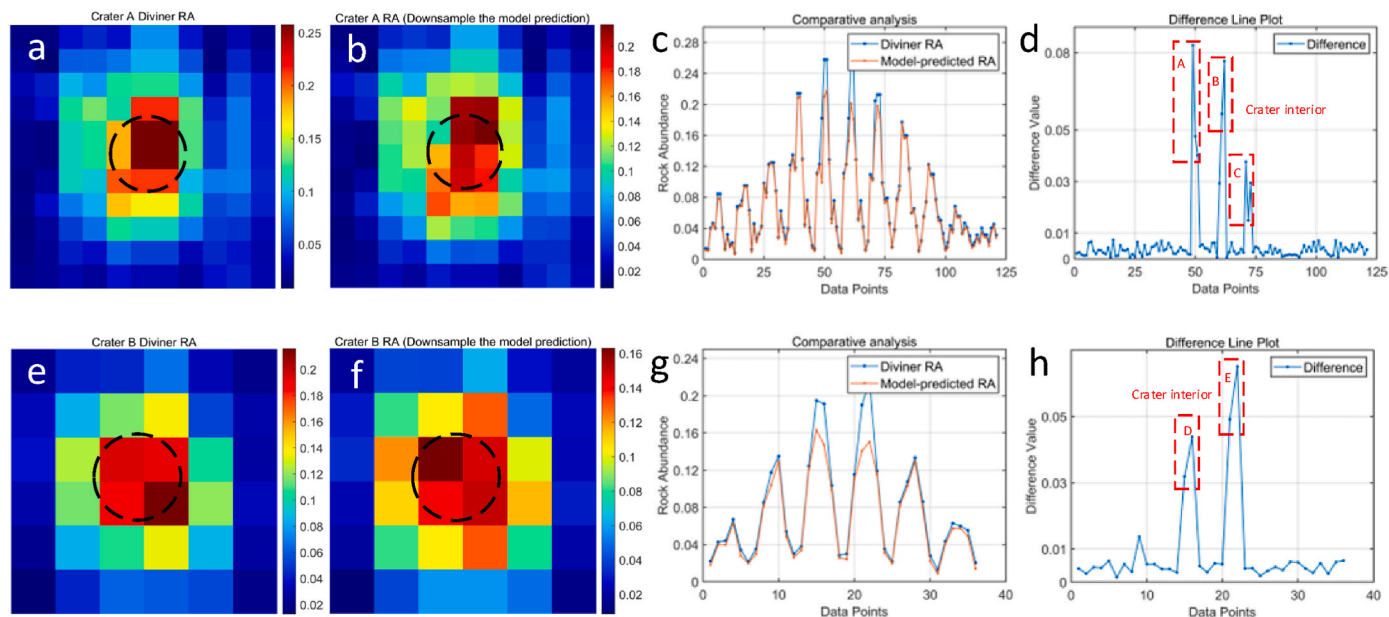


Fig. 16. (a) and (e) represent the Diviner RA for Crater A and Crater B, respectively. (b) and (f) show the model-derived RA for the same craters. (c) and (g) present a row-priority comparative analysis between the Diviner RA and the model-derived RA for both craters. (d) and (h) represent the difference between these two datasets. The red boxes in (d) and (h) highlight the crater interiors.

Table 5

Comparison of overall accuracy and RMSE between model-derived rock abundance and Diviner data.

| | Crater A | Crater B |
|----------------|----------|----------|
| Model Accuracy | 93.14 % | 90.73 % |
| RMSE | 0.0143 | 0.017 |

derivation methods based solely on optical data, the RA-SAR model provides more convenient and detailed information on rock distribution.

In terms of error analysis, while the RA-SAR model performs well overall, certain sources of error remain. The resolution of SAR data limits the detection of smaller rocks, particularly at the edges of smaller craters (Liu and Jin, 2021). In validation against optical data, the complementarity between SAR and optical data becomes evident, as optical data provide more intuitive surface information.

As for the model's limitations, although the RA-SAR model demonstrates excellent performance in cold spot crater derivation, its applicability has certain constraints. Specifically,

1. The spatial resolution limitations of SAR data may result in inaccuracies in capturing fine-scale rock distribution features, thereby affecting the precise estimation of rock abundance.
2. The surface roughness and dielectric properties of the lunar regolith can also influence the SAR backscatter signal, leading to potential errors in the rock abundance estimation.
3. Due to the absence of sampling within crater interiors during model construction, combined with the interference from the complex topography of the crater walls, the SAR-derived rock abundance within the craters may involve relatively large errors.
4. Although the model performs well in estimating rock abundance for lunar cold spot craters, its performance may be less reliable for craters that are degraded or lack surface rock exposures.

In addition, the model's accuracy may diminish in regions lacking significant thermal inertia features. Nevertheless, the high-resolution RA derivation presented in this study offers crucial data for understanding the formation and evolution of cold spot craters. Especially in regions where thermal inertia features are closely tied to RA, accurate RA data can further elucidate geological processes on the lunar surface. Our model also lays the groundwork for future lunar exploration

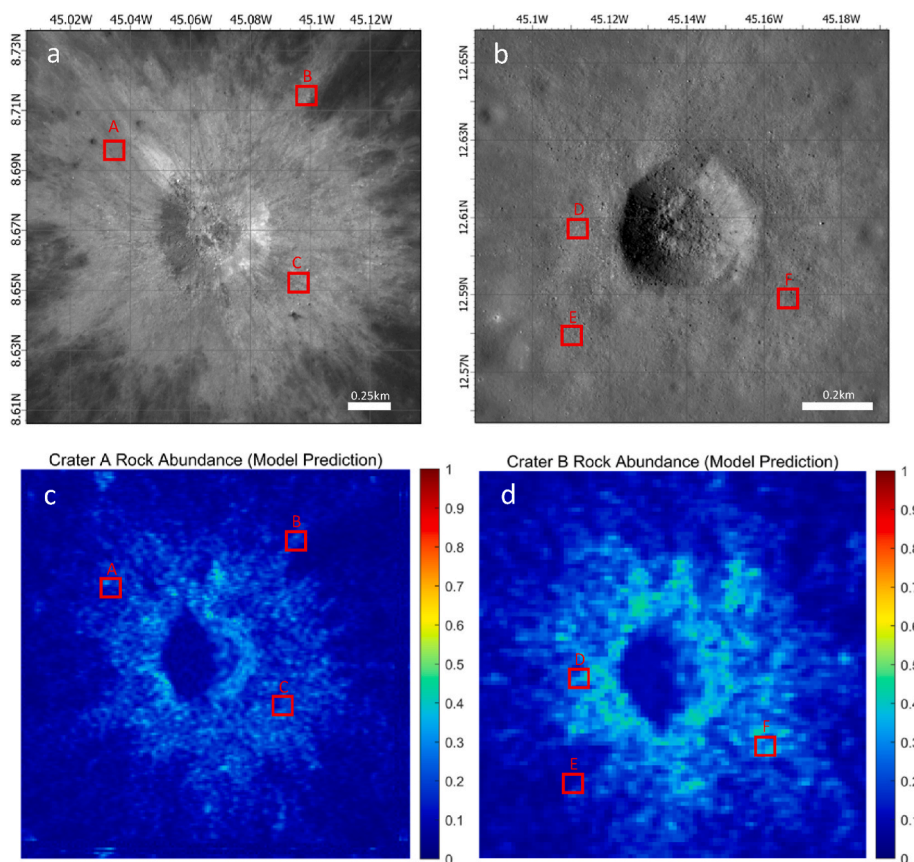


Fig. 17. (a) and (b) show the optical images of Crater A and Crater B, respectively, while (c) and (d) present the model-derived high-resolution RA. The red boxes in the images indicate the randomly selected validation regions.

Table 6

The accuracy evaluation results of RA for the randomly selected regions a, b, c, d, e and f using optical images.

| The selected region of Crater A | Accuracy | The selected region of Crater B | Accuracy |
|---------------------------------|----------|---------------------------------|----------|
| a | 91.86 % | d | 92.25 % |
| b | 89.11 % | e | 89.74 % |
| c | 93.24 % | f | 90.12 % |

missions, aiding in the identification and analysis of potential landing sites and scientific investigation targets.

6. Conclusion

This study established a high-resolution RA derivation model for lunar cold spot craters, based on Mini-RF SAR data and LROC NAC optical data. By analyzing the correlation between the Stokes parameters and optically derived RA data, we developed a robust RA-SAR model. This model allows for the accurate derivation of RA in other lunar cold spot craters. The results demonstrate that the linear regression model between SAR parameters and RA provides a reliable method for predicting rock abundance in lunar cold spot craters. Our findings highlight the significant potential of using SAR data to infer surface characteristics in environments where optical data are limited.

Overall, the RA-SAR model opens new avenues for planetary surface analysis and enhances our understanding of lunar crater formation and evolution. Future work may focus on improving the model’s accuracy by incorporating additional data sources or extending its application to other planetary bodies. The methodology proposed in this study provides a valuable framework for remote sensing research in planetary

science, particularly for analyzing regions with complex geological features.

CRediT authorship contribution statement

Jiacheng Sun: Writing – original draft, Visualization, Validation, Software, Methodology, Formal analysis, Conceptualization. **Xin Lu:** Writing – original draft, Visualization, Validation, Resources, Data curation. **Gaofeng Shu:** Writing – review & editing, Writing – original draft, Supervision, Methodology, Investigation, Conceptualization. **Zhengwei Guo:** Writing – review & editing, Validation, Supervision, Data curation. **Ning Li:** Writing – review & editing, Validation, Supervision, Resources.

Author statement/agreement

All authors have seen and approved the final version of the manuscript being submitted. They warrant that the article is the authors’ original work, hasn’t received prior publication, and isn’t under consideration for publication elsewhere.

Declaration of competing interest

The authors declare that they have no known competing financial interests or personal relationships that could have appeared to influence the work reported in this paper.

Data availability

The LROC NAC optical data and Mini-RF SAR data used in this study are publicly available from the Lunar Orbital Data Explorer

(<https://ode.rsl.wustl.edu/moon>). The Diviner data products used are publicly available via the Geosciences Node of the Planetary Data System (<https://pds-geosciences.wustl.edu/missions/lro/diviner.htm>).

References

- Bandfield, J.L., et al., 2011. Lunar surface rock abundance and regolith fines temperatures derived from LRO Diviner Radiometer data. *J. Geophys. Res.: Planets* 116 (E12). <https://doi.org/10.1029/2011JE003866>.
- Bandfield, J.L., Song, E., Hayne, P.O., et al., 2014. Lunar cold spots: granular flow features and extensive insulating materials surrounding young craters. *Icarus* (New York, N. Y., 1962) 231, 221–231. <https://doi.org/10.1016/j.icarus.2013.12.017>.
- Bandfield, J.L., Cahill, J.T.S., Carter, L.M., et al., 2017. Distal ejecta from lunar impacts: extensive regions of rocky deposits. *Icarus* (New York, N. Y., 1962) 283, 282–299. <https://doi.org/10.1016/j.icarus.2016.05.013>.
- Bart, G.D., Melosh, H.J., 2010a. Impact into lunar regolith inhibits high-velocity ejection of large blocks. *J. Geophys. Res.: Planets* 115 (E8). <https://doi.org/10.1029/2009JE003441>.
- Bart, G.D., Melosh, H.J., 2010b. Distributions of boulders ejected from lunar craters. *Icarus* (New York, N. Y., 1962) 209 (2), 337–357. <https://doi.org/10.1016/j.icarus.2010.05.023>.
- Cahill, J.T.S., Thomson, B.J., Patterson, G.W., et al., 2014. The miniature radio frequency instrument's (Mini-RF) global observations of Earth's Moon. *Icarus* (New York, N. Y., 1962) 243, 173–190. <https://doi.org/10.1016/j.icarus.2014.07.018>.
- Calla, O.P.N., Mathur, S., Jangid, M., et al., 2015. Circular polarization characteristics of south polar lunar craters using Chandrayaan-1 Mini-SAR and LRO Mini-RF. *Earth Moon Planets* 115, 83–100. <https://doi.org/10.1007/s11038-015-9469-7>.
- Campbell, B.A., 2012. High circular polarization ratios in radar scattering from geologic targets. *J. Geophys. Res.: Planets* 117 (E6). <https://doi.org/10.1029/2012JE004061>.
- Carter, L.M., Neish, C.D., Bussey, D.B.J., et al., 2012. Initial observations of lunar impact melts and ejecta flows with the Mini-RF radar. *J. Geophys. Res.: Planets* 117 (E12). <https://doi.org/10.1029/2011JE003911>.
- Carter, L.M., Campbell, B.A., Neish, C.D., et al., 2017. A comparison of radar polarimetry data of the Moon from the LRO Mini-RF instrument and Earth-based systems. *IEEE Trans. Geosci. Rem. Sens.* 55 (4), 1915–1927. <https://doi.org/10.1109/TGRS.2016.2631144>.
- Cintala, M.J., Head, J.W., Veverka, J., 1978. Characteristics of the cratering process on small satellites and asteroids. In: *Lunar and Planetary Science Conference, 9th, Houston, TX, March 13-17, 1978, Proceedings*. Pergamon Press, New York, pp. 3803–3830.
- Elder, C.M., Hayne, P.O., Bandfield, J.L., et al., 2017. Young lunar volcanic features: thermophysical properties and formation. *Icarus* (New York, N. Y., 1962) 290, 224–237. <https://doi.org/10.1016/j.icarus.2017.03.004>.
- Elder, C.M., Douglass, B., Ghent, R.R., et al., 2019. The subsurface coherent rock content of the moon as revealed by cold-spot craters. *J. Geophys. Res.: Planets* 124 (12), 3373–3384. <https://doi.org/10.1029/2019JE006128>.
- Fa, W., Cai, Y., 2013. Circular polarization ratio characteristics of impact craters from Mini-RF observations and implications for ice detection at the polar regions of the Moon. *J. Geophys. Res.: Planets* 118 (8), 1582–1608. <https://doi.org/10.1002/jgrg.20110>.
- Fa, W., Wiczorek, M.A., 2012. Regolith thickness over the lunar nearside: results from Earth-based 70-cm Arecibo radar observations. *Icarus* (New York, N. Y., 1962) 218 (2), 771–787. <https://doi.org/10.1016/j.icarus.2012.01.010>.
- Gao, Y., Zhao, F., Hou, W., et al., 2023. Analysis of rock abundance on lunar surface and near-surface using Mini-RF SAR data. *IEEE J. Sel. Top. Appl. Earth Obs. Rem. Sens.* 16, 9590–9605. <https://doi.org/10.1109/JSTARS.2023.3323510>.
- Ghent, R.R., Hayne, P.O., Bandfield, J.L., et al., 2014. Constraints on the recent rate of lunar ejecta breakdown and implications for crater ages. *Geology* 42 (12), 1059–1062. <https://doi.org/10.1130/G35926.1>.
- Hayne, P.O., Bandfield, J.L., Siegler, M.A., et al., 2017. Global regolith thermophysical properties of the moon from the diviner lunar radiometer experiment. *J. Geophys. Res.: Planets* 122 (12), 2371–2400. <https://doi.org/10.1002/2017JE005387>.
- Head, J.W., Fassett, C.I., Kadish, S.J., Smith, D.E., Zuber, M.T., Neumann, G.A., Mazarico, E., 2010. Global distribution of large lunar craters: implications for resurfacing and impactor populations. *Science* 329 (5998), 1504–1507. <https://doi.org/10.1126/science.1195050>.
- Hiesinger, H., Head III, J.W., Wolf, U., et al., 2003. Ages and stratigraphy of mare basalts in Oceanus Procellarum, mare nubium, mare cognitum, and mare insularum. *J. Geophys. Res.: Planets* 108 (E7). <https://doi.org/10.1029/2002JE001985>.
- Hörz, F., Grieve, R., Heiken, G., Spudis, P., Binder, A., 1991. *Lunar Sourcebook - A User's Guide to the Moon*. Cambridge University Press, pp. 61–111.
- Housen, K.R., Schmidt, R.M., Holsapple, K.A., 1983. Crater ejecta scaling laws: fundamental forms based on dimensional analysis. *J. Geophys. Res. Solid Earth* 88 (B3), 2485–2499. <https://doi.org/10.1029/JB088iB03p02485>.
- Huang, Z., Song, Z., Shu, G., et al., 2023. Removing the effect of lunar topography on Mini-RF SAR polarimetric parameters through DEM data. *Geosci. Rem. Sens. Lett. IEEE*. <https://doi.org/10.1109/LGRS.2023.3343116>.
- Kumari, H., Bhardwaj, A., 2020. Analysis of polarimetric Mini-SAR and Mini-RF datasets for surface characterization and crater delineation on Moon. *Environmental Sciences Proceedings* 4 (1), 10. <https://doi.org/10.3390/ecas2020-08118>.
- Liu, N., Jin, Y.Q., 2021. Simulation of Pol-SAR imaging and data analysis of Mini-RF observation from the lunar surface. *IEEE Trans. Geosci. Rem. Sens.* 60, 1–11. <https://doi.org/10.1109/TGRS.2021.3064091>.
- McKay, D.S., Heiken, G., Basu, A., et al., 1991. The lunar regolith. In: Hörz, F., Grieve, R., Heiken, G., Spudis, P., Binder, A. (Eds.), *Lunar Sourcebook - A User's Guide to the Moon*. Cambridge University Press, pp. 285–356.
- Mustard, J.F., Pieters, C.M., Isaacson, P.J., et al., 2011. Compositional diversity and geologic insights of the Aristarchus crater from Moon Mineralogy Mapper data. *J. Geophys. Res.: Planets* 116 (E6). <https://doi.org/10.1029/2010JE003726>.
- Neish, C.D., Bussey, D.B.J., Spudis, P., et al., 2011. The nature of lunar volatiles as revealed by Mini-RF observations of the LCROSS impact site. *J. Geophys. Res.: Planets* 116 (E1). <https://doi.org/10.1029/2010JE003647>.
- Neish, C.D., Madden, J., Carter, L.M., et al., 2014. Global distribution of lunar impact melt flows. *Icarus* (New York, N. Y., 1962) 239, 105–117. <https://doi.org/10.1016/j.icarus.2014.05.049>.
- Nozette, S., Spudis, P., Bussey, B., et al., 2010. The lunar reconnaissance orbiter miniature radio frequency (Mini-RF) technology demonstration. *Space Sci. Rev.* 150, 285–302. <https://doi.org/10.1007/s11214-009-9607-5>.
- Paige, D.A., et al., 2010. The lunar reconnaissance orbiter Diviner lunar radiometer experiment. *Space Sci. Rev.* 150, 125–160. <https://doi.org/10.1007/s11214-009-9529-2>.
- Paige, D., Sullivan, M., Williams, J.P., 2022. Lunar Reconnaissance Orbiter Diviner Derived Data Bundle 1, vol. 26. NASA Planetary Data System. <https://doi.org/10.17189/WJOS-W188>.
- Powell, T.M., et al., 2023. High-resolution nighttime temperature and rock abundance mapping of the Moon using the Diviner Lunar Radiometer Experiment with a model for topographic removal. *J. Geophys. Res.: Planets* 128 (2), e2022JE007532. <https://doi.org/10.1029/2022JE007532>.
- Raney, R.K., 2006. Dual-polarized SAR and Stokes parameters. *Geosci. Rem. Sens. Lett. IEEE* 3 (3), 317–319. <https://doi.org/10.1109/LGRS.2006.871746>.
- Raney, R.K., 2019. Hybrid dual-polarization synthetic aperture radar. *Remote Sens.* 11 (13), 1521. <https://doi.org/10.3390/rs11131521>.
- Raney, R.K., Spudis, P.D., Bussey, B., et al., 2010. The lunar Mini-RF radars: hybrid polarimetric architecture and initial results. *Proc. IEEE* 99 (5), 808–823. <https://doi.org/10.1109/JPROC.2010.2084970>.
- Richardson, J.E., Melosh, H.J., Artemeva, N.A., et al., 2005. Impact cratering theory and modeling for the Deep Impact mission: from mission planning to data analysis. *Space Sci. Rev.* 117, 241–267. <https://doi.org/10.1007/s11214-005-3393-5>.
- Robinson, M.S., Brylow, S.M., Tschimmel, M., et al., 2010. Lunar reconnaissance orbiter camera (LROC) instrument overview. *Space Sci. Rev.* 150, 81–124. <https://doi.org/10.1007/s11214-010-9634-2>.
- Stöffler, D., Ryder, G., Ivanov, B.A., et al., 2006. Cratering history and lunar chronology. *Rev. Mineral. Geochem.* 60 (1), 519–596. <https://doi.org/10.2138/rmg.2006.60.05>.
- Venkatraman, J., Horvath, T., Powell, T.M., et al., 2023. Statistical estimates of rock-free lunar regolith thickness from Diviner. *Planet. Space Sci.* 229, 105662. <https://doi.org/10.1016/j.pss.2023.105662>.
- Wagner, R.V., Henriksen, M.R., Manheim, M.R., et al., 2024. Where is that crater? Best practices for obtaining accurate coordinates from LROC NAC data. *The Planetary Science Journal* 5 (7), 157. <https://doi.org/10.3847/PSJ/ad54c6>.
- Williams, J.-P., et al., 2017. The global surface temperatures of the moon as measured by the diviner lunar radiometer experiment. *Icarus* (New York, N. Y., 1962) 283, 300–325. <https://doi.org/10.1016/j.icarus.2016.08.012>.
- Williams, J.P., Bandfield, J.L., Paige, D.A., et al., 2018. Lunar cold spots and crater production on the moon. *J. Geophys. Res.: Planets* 123 (9), 2380–2392. <https://doi.org/10.1029/2018JE005652>.
- Wu, B., Liu, W.C., 2017. Calibration of boresight offset of LROC NAC imagery for precision lunar topographic mapping. *ISPRS J. Photogrammetry Remote Sens.* 128, 372–387. <https://doi.org/10.1016/j.isprsjprs.2017.04.012>.
- Wu, B., Hu, H., Liu, W.C., 2018. Photogrammetric processing of LROC NAC images for precision lunar topographic mapping. In: *Planetary Remote Sensing and Mapping*. CRC Press, pp. 125–147. <https://doi.org/10.1201/9780429505997-10>.
- Zhang, C., Chen, J., Pan, Y., et al., 2024. Geomorphology, mineralogy, and chronology of mare basalts in the Oceanus Procellarum region. *Remote Sens.* 16 (4), 634. <https://doi.org/10.3390/rs16040634>.